Characterization of Solid State Phase Transformation in Continuously Heated and Cooled Ferritic Weld Metal

B. Narayanan, M. J. Mills, E. D. Specht, M. L. Santella and S. S. Babu

1 Introduction

Arc welding processes involve cooling rates that vary over a wide range (1–100 K/s). The final microstructure is thus a product of the heating and cooling cycles experienced by the weld in addition to the weld composition. It has been shown that the first phase to form under weld cooling conditions may not be that predicted by equilibrium calculations (Babu et al. 2002a). The partitioning of different interstitial/substitutional alloying elements at high temperatures can dramatically affect the subsequent phase transformations. In order to understand the effect of alloying on phase transformation temperatures and final microstructures time-resolved X-ray diffraction technique has been successfully used for characterization (Babu et al. 2002a, 2005; Stone et al. 2008; Babu 2002). The work by Jacot and Rappaz (1999) on pearlitic steels provided insight into austenitization of hypo-eutectic steels using a finite volume model. However there is very little work done on the effect of heating and cooling rates on the phase transformation paths in bainitic/martensitic steels and weld metals (Thiessen et al. 2007). Previous work on a weld with higher aluminum content, deposited with a FCAW-S process indicated that even at aluminum levels where the primary phase to solidify from liquid should be delta ferrite, non-equilibrium austenite was observed (Babu 2002). The presence of inhomogeneity in composition of the parent microstructure has been attributed to differences in transformation modes, temperatures and microstructures in dual-phase, TRIP steels and ferritic welds (Jimenez-Melero

B. Narayanan (✉)
Lincoln Electric Company, Cleveland OH, USA
e-mail: Badri_Narayanan@lincolnelectric.com

M. J. Mills and S. S. Babu
The Ohio State University, Columbus OH, USA

E. D. Specht and M. L. Santella
Oak Ridge National Laboratory, Columbus OH, USA

T. Kannengiesser et al. (eds.), *In-situ Studies with Photons, Neutrons and Electrons Scattering*, DOI: 10.1007/978-3-642-14794-4_7,
© Springe-Verlagr Berlin Heidelberg 2010

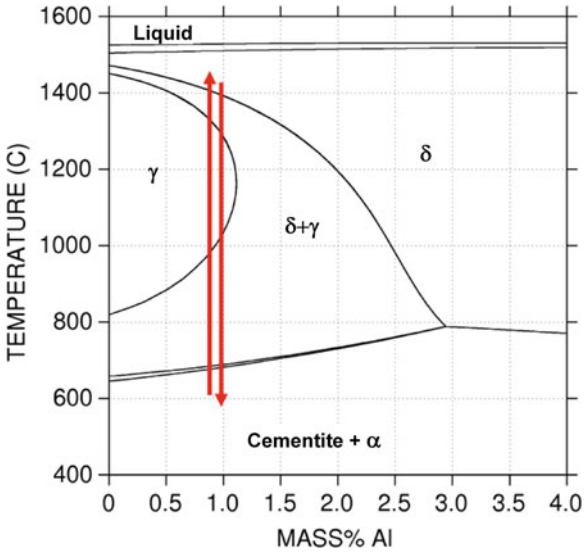

Fig. 1 Pseudo-binary phase diagram of the weld composition. The transformation path is indicated

et al. 2009; Wang and Van Der Zwaag 2001; Babu et al. 2002b; Palmer and Elmer 2005).

The objectives of the work included the identification of the stability regions of different phases during heating and cooling, differences in the effect of weld heating and cooling rates on the phase transformation temperatures, and the variation in phase fractions of austenite and ferrite in the two phase regions as a function of temperature. The base composition used for the present work is a Fe–1%Al–2%Mn–1%Ni–0.04%C weld metal. A pseudo-binary phase diagram (Fig. 1) shows the expected solidification path under equilibrium conditions. However, the effect of heating and cooling rates on the phase transformation path due to non-equilibrium partitioning of alloying elements cannot be predicted by equilibrium phase diagrams. Also, it is unclear if there is retention of delta ferrite to room temperature due to compositional or thermal effects. This would dramatically affect the austenite to ferrite transformation due to carbon and nitrogen enrichment in the austenite.

2 Experimental Procedure

A 2.0 mm FCAW-S electrode was used to make a multi-pass weld. The joint configuration and the corresponding micro-hardness map are shown in Fig. 2a–b. Thermocouples were plunged in the weld pool during welding to determine cooling rates. An S-type (Pt–Pt/Rh) thermocouple was plunged into the weld pool and the data logged using a Labview^{TM} data acquisition system. The chemical composition of the weld metal was determined using an emission spectrometer.

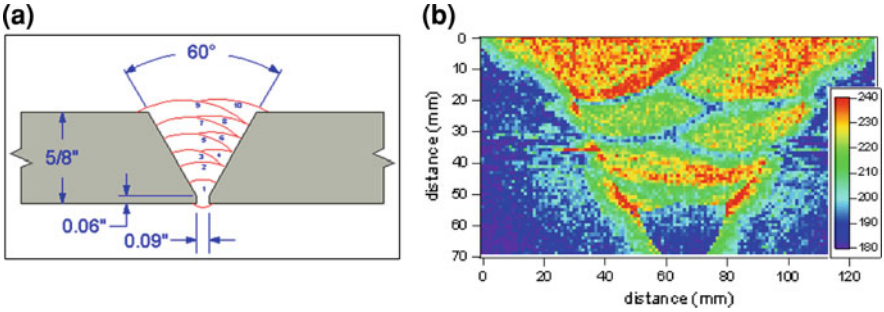

Fig. 2 **a** Joint configuration indicating the region of interest and **b** corresponding microhardness map of the weld

Magnesium was measured using an inductively coupled plasma in conjunction with a mass spectrometer. Carbon was measured using a LECO CS244 carbon analyzer while oxygen and nitrogen measurements were analyzed using a LECO TC436DR O/N analyzer. The as-welded region of the weld metal was characterized using electron backscattered diffraction (EBSD) in conjunction with orientation imaging microscopy (OIM). A XL-30 ESEM equipped with a FEG source and a TSL electron backscatter pattern and phase identification system was used in the present work. The scans were set-up to run with a step size between 0.2 and 0.5 μm. A confidence index filter of 0.15 was used for all analysis. Samples extracted from the as-deposited region were ground to thickness of approximately 200 μm. These samples were then cut into 3 mm discs, polished down to 100 μm and electro-polished in a Struers Tenupol-3 twin-jet electropolisher using 10% perchloric acid and 90% acetic acid as the electrolyte. The applied voltage was 12 V and samples were electropolished at room temperature. Conventional transmission electron microscopy (CTEM) and annular dark field (ADF) scanning transmission electron microscopy (STEM) techniques were used to analyze and characterize the solidification structure using a Tecnai F-20 FEG/TEM at 200 kV operating voltage.

Rectangular samples (2 mm × 4 mm × 95 mm) were taken from the as-welded region of the multi-pass weld. The samples were EDM machined and polished to get rid of any mechanical damage to the surface. The experimental set-up is identical to that discussed in (Babu et al. 2005) and shown in Fig. 3a. The details of the set-up are as follows. The samples were heated in situ using a resistive heater attached to the ends of the sample as shown in Fig. 3b. A type S (Pt/Pt–Rh) thermo-couple was spot welded to the back of the sample to monitor and control the temperature. The sample was kept in an argon environment to prevent oxidation. Two different heating and cooling rates were employed (10 and 5°C/s) and taken up to a maximum temperature of 1450°C. Bending magnet synchrotron radiation was provided by beam line ×33-BM-B at the Advanced Photon Source (Argonne, IL, USA). A 30 keV X-ray source was used with a double-crystal Si (111) monochromator. The sample was positioned such that the uniformly heated

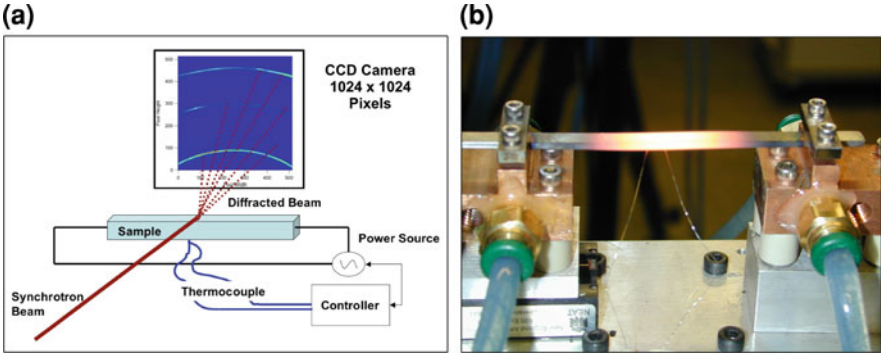

Fig. 3 **a** Schematic of the experimental set-up. **b** Actual experimental set-up showing the attachment of thermocouple and the resistive heating of the sample

region was at a glancing angle of 5° to the incident X-rays. The diffracted intensities were measured using a Peltier cooled 2-D area CCD detector. The instrument resolution is estimated to be 0.005–0.015 Å for an inter-planar spacing between 0.5 and 2.5 Å, respectively. The minimum time resolution with this set-up for an acceptable signal to noise ratio is estimated to be 3 s. This constraint limited the heating and cooling rates to 10°C/s as increased rates will lead to "averaging" of the data collected (i.e. If the sample is heated at 10°C/s, the signal is averaged over 30°C). Diffracted X-rays were collected over a 1.1–2.4 Å d-spacing range that collected the {112}, {002} and {011} ferrite and the {111}, {002} and {022) austenite reflections. The intensities were collected using a 2-D area detector. The 2-D area detector collects X-rays over a wider solid angle and is advantageous over a 1-D detector to improve counting statistics (Hammersley et al. 1995). The intensities are normalized on a scale of 0–1 and the relative intensities of the different peaks measured. The peak intensity, full width at half maximum, integrated intensities, and peak position were tabulated. The integrated intensity (I) and the full width at half maximum (FWHM) was calculated after fitting the peaks to a Gaussian function.

3 Calculation of Phase Fraction of Austenite and Ferrite as a Function of Temperature

The austenite {111} and ferrite {011} peaks were used to calculate relative phase fractions using the Cullity method (1978). The phase fraction calculation was determined from the relative intensities of the {111} austenite and {110} ferrite peaks. The relative integrated intensity of a particular $\{hkl\}$ plane is given by (1)

$$I_{\{hkl\}} = \left|F_{\{hkl\}}\right|^2 \times m \times \left(\frac{1+\cos^2 2\theta}{\sin^2\theta \cdot \cos\theta}\right) \times \exp(-2M) \quad (1)$$

where $F_{\{hkl\}}$ is the structure factor of the $\{hkl\}$ set of planes, m is the multiplicity factor, θ is the bragg angle, and exp(−2M) is the Debye–Waller factor. The structure factors are

$$\left|F_{\gamma}\right|^2 = (4f)^2 \quad \text{and} \quad |F_{\alpha}|^2 = (2f)^2 \tag{2}$$

for austenite and ferrite, respectively, where 'f' is the atomic scattering factor for an atom of iron. For the calculation of relative phase fractions of austenite and ferrite, the effects due to absorption and temperature are assumed to cancel each other out and the ratio of the intensities thus obtained gives the relative phase fractions of the two phases.

These samples subjected to the thermal cycles were then polished and etched using a Beraha reagent (sodium metabisulfite + potassium metabisulfite in an aqueous solution) and the microstructures characterized using a Zeiss optical microscope. The microstructure was further characterized using scanning electron microscopy in conjunction with energy dispersive X-ray spectroscopy.

Dictra™ (Andersson 2002), a software package that can simulate multi-component diffusion was used to model the effect of heating and cooling rates to determine phase transformation temperatures and regions of stability of ferrite and austenite.

4 Results

Chemical Composition

The weld metal composition is shown in Table 1 below.

Weld Microstructure Characterization

The microstructure of the as-welded region is shown in Fig. 4 as a color coded inverse pole figure (IPF). The prior austenitic grain size is of the order of 100 μm in width. The IPF's provide information on the orientation of the individual blocks of ferrite. There are also small pockets of retained austenite present in the weld. The pole figures of the austenite and ferrite corresponding to Fig. 4a are shown in Fig. 4b, c. These pole figures suggest that the orientation relationship between the ferrite and austenite is close to a Kurdjumov–Sachs orientation relationship.

Table 1 Chemical composition of weld for in situ synchrotron diffraction characterization

	C	Al	Mn	O	N	Ni	Mg*	Ti	Zr	Si
Weld	0.02	0.9	2.0	0.01	0.02	0.8	0.01	0.03	0.04	0.15

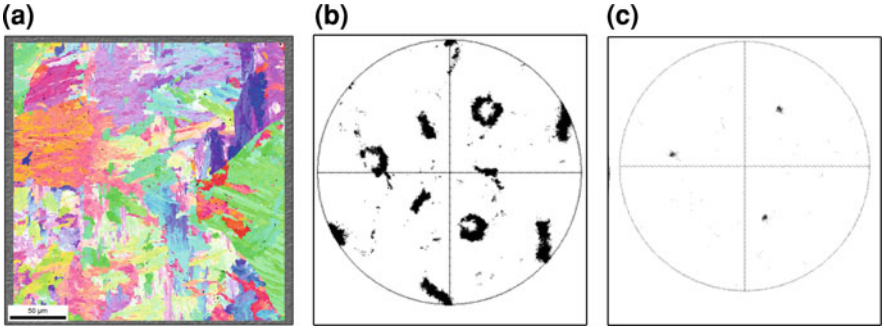

Fig. 4 **a** Inverse pole figure showing orientation of ferrite laths in the as-welded region. **b** [001] Pole figure showing K–S O.R. of ferrite laths within a prior austenitic grain. **c** [001] Pole figure of retained austenite corresponding to **b**

Fig. 5a shows an ADF-STEM image of retained austenite (RA). The corresponding BF-STEM image (Fig. 5b) also shows that these austenitic regions had transformed partially to martensite (M). EDS line profiles (Fig. 5c) across these RA + M regions did not show a difference in partitioning of alloying elements.

The microstructures of the samples after thermal cycling were observed optically after etching with a Beraha etchant. Figure 6a and b shows the microstructures after thermal cycling. The prior austenitic grains for the 10°C/s thermal cycle and the 5°C/s thermal cycle treatment were more polygonal in shape than the base microstructure. The prior austenitic grain sizes were $\sim 127 \pm 31$ μm for the 10°C/s and $\sim 97 \pm 26$ μm for the 5°C/s thermal cycle. EDS analysis of the samples after thermal cycling did not show any signs of chemical segregation except for aluminum enriched regions which correlated spatially with the presence of inclusions in the weld.

X-Ray Synchrotron Characterization

Figure 7a and b shows the diffraction peak intensities in the form of an intensity map along with the temperature profile for the sample heated and cooled at 10 and 5°C/s, respectively. The transformation from room temperature alpha ferrite to delta ferrite at the peak temperature of 1450°C upon heating and back to alpha ferrite upon cooling is apparent from the shifts in peak intensities. The lattice parameter of the alpha ferrite is taken to be 2.866 Å from room temperature X-ray diffraction measurements. There was a systematic error in the peak positions in the synchrotron experiment in comparison to the room temperature XRD data. The peak positions were corrected for this systematic shift in peak positions. Figure 8a and b shows the phase fractions of austenite and ferrite obtained as a function of temperature during heating and cooling, respectively.

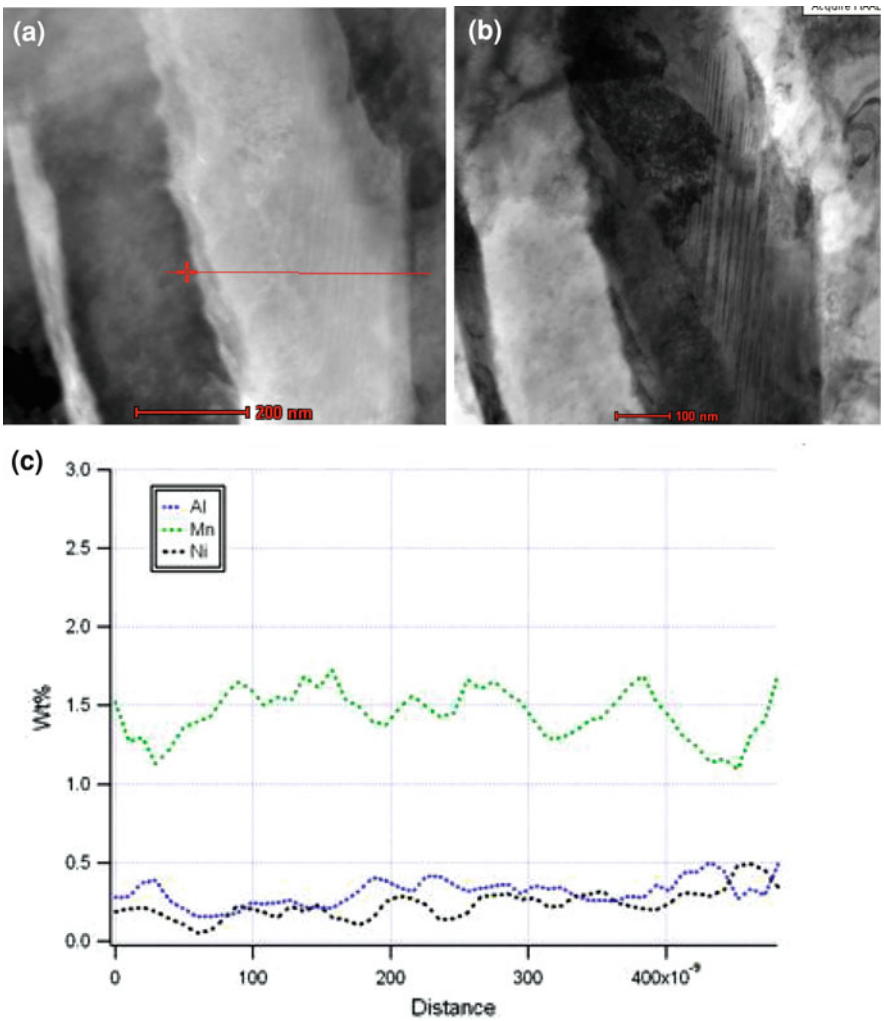

Fig. 5 **a** DF-STEM image of a retained austenitic region, **b** BF-STEM image of the same region showing a mixture of austenite and martensite. **c** EDS line profile corresponding to the *line marker* shown in **a**

The samples on heating did not show any difference between the two different rates of heating in terms of transformation temperatures. Both samples on heating go through single phase austenite and transform completely to delta ferrite. The ferrite to austenite transformation goes to completion around 934°C. The austenite to delta ferrite transformation starts at 1330°C and goes to completion at 1400°C. The samples were heated to a peak temperature of 1450°C and cooled at the same rate at which they were heated. Upon cooling there is a measurable and significant difference in the transformation temperature of the delta to gamma phase

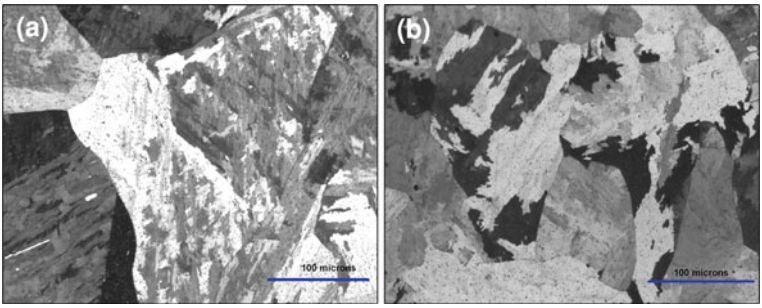

Fig. 6 Optical microstructure of the weld subjected to a **a** 10°C/s and **b** 5°C/s thermal cycle

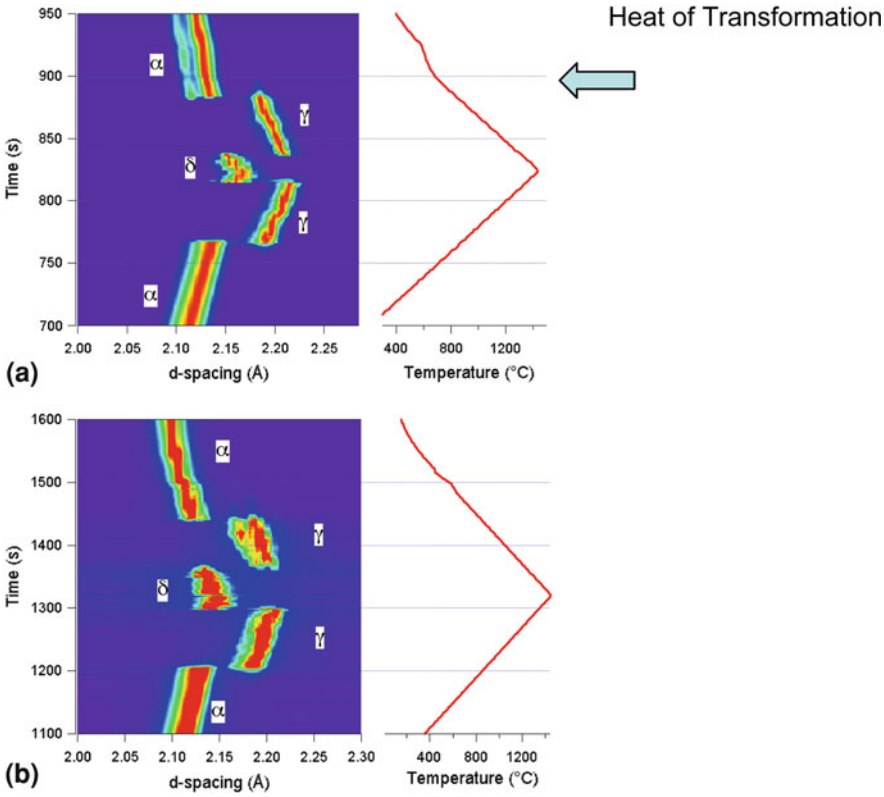

Fig. 7 Phase evolution and temperature profile during heating and cooling at 10°C/s **a** and 5°C/s **b**, respectively

transformation. The transformation begins at a higher temperature (1342°C) at the faster cooling rate of 10°C/s in comparison to 1280°C at the slower cooling rate of 5°C/s. The austenite to ferrite transformation at both cooling rates occurs at 860–880°C.

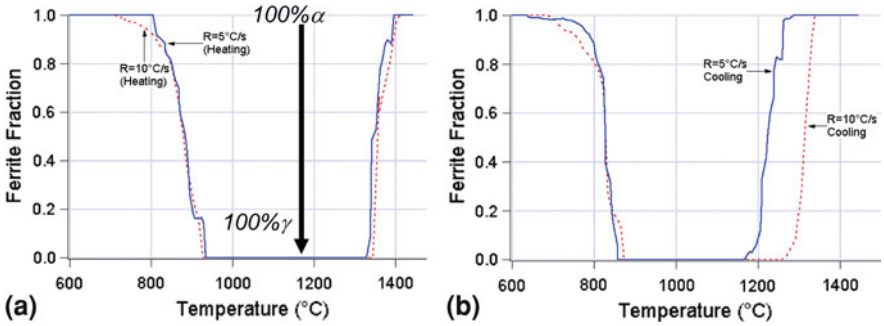

Fig. 8 Ferrite/Austenite phase evolution during heating and cooling at **a** 5°C/s and **b** 10°C/s

These results indicate that there is a significant effect of cooling rates on the delta to gamma transformation temperature. The difference in the transformation temperature between the two different thermal cycles is 62°C, which cannot be attributed to experimental conditions. As stated previously, there is an averaging of the signals obtained due to the limitations of the data acquisition system. This could account for approximately 15°C of the differences in transformation temperatures between the fast and slow thermal cycles. However, it is not possible to explain a difference of 62°C entirely due to measurement system artifacts. Also, there should have been a similar shift seen during heating if this was related to the rate of data acquisition.

5 Discussion

The delta to gamma transformation at high temperatures should be diffusion controlled and the transformation temperature is expected to be suppressed to lower temperatures with increase in cooling rates contrary to what is observed in the experimental results. This was simulated using Dictra to understand the effect of cooling rates on transformation temperatures.

Diffusion Controlled Growth Simulation of Gamma from Delta During Cooling

The simulation of the delta to gamma transformation was done using TCFE5 or SSOL2 and MOBILITY database using Dictra^{TM}. The elements used in the simulation are Fe, Al, Mn and C. The cooling rate was varied (5, 10, 15, 30°C/s). A 10 μm ferrite cell was made the active phase with the austenite being the inactive phase. The starting composition was chosen to be the bulk composition of

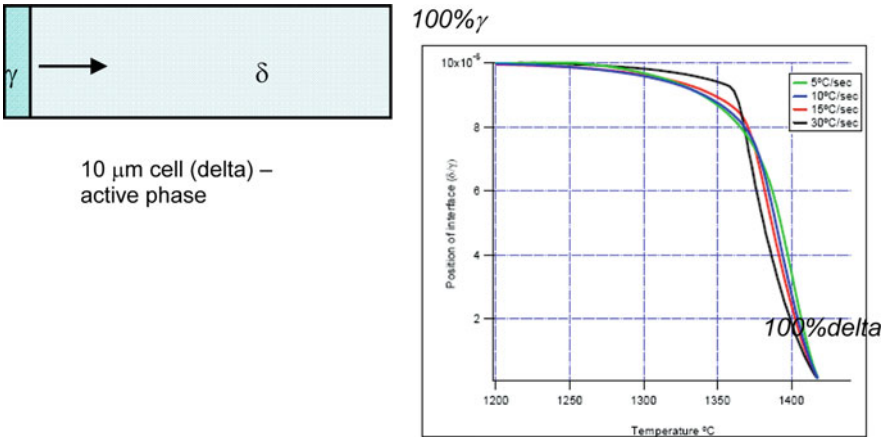

Fig. 9 Dictra simulation of phase transformation at different cooling rates from delta ferrite to austenite

the weld (1%Al, 2%Mn, 0.03%C). The starting temperature was 1500°C and was cooled to the single phase austenite at the different cooling rates. The position of the interface (austenite/ferrite) is plotted as a function of temperature to compare the effect of cooling rate (Fig. 9). There was no significant change in the transformation start temperatures between the different cooling rates. Since nucleation of the new phase is not accounted for in the calculations, the transformation start temperature is invariant. The trend in simulated growth rate with decreasing temperature is consistent with diffusion controlled growth. It is known that the supersaturation ahead of the transforming interface and diffusivity controls growth rate. The effect of faster cooling rate is to cause higher undercooling thus increasing the rate of growth initially until the diffusivity of mobile species slows down enough to control the growth rate. The simulations, however, show no difference in the temperature range ($\sim$80°C) of the two phase ($\delta + \gamma$) region between the two cooling rates. There are two alternate hypotheses that could account for this difference in transformation temperatures.

Compositional Heterogeneity in Delta Due to Faster Heating Rate

As a first step, the extent of compositional heterogeneity that could induce a shift of 62°C in transformation temperatures is ascertained. Thermo-Calc was used to measure the potency of the different alloying additions on the delta to gamma transformation temperature. Aluminum is a ferrite stabilizer and decreases the transformation temperature of delta to gamma while manganese and nickel increase the transformation temperature. The thermodynamic calculations suggest

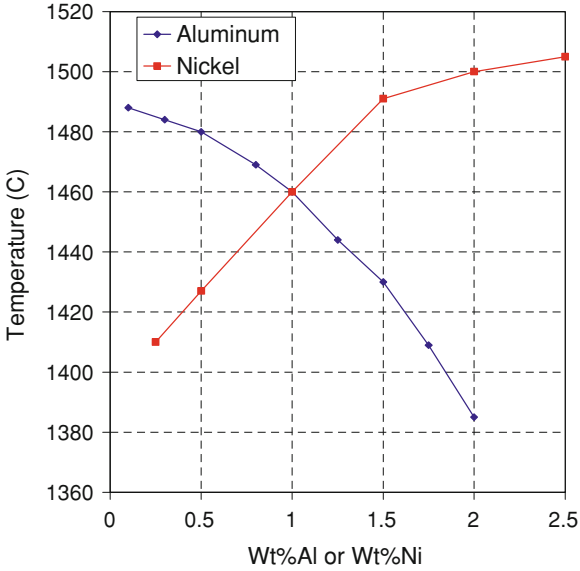

Fig. 10 Effect of alloying on delta to gamma transformation temperature predicted by Thermo-Calc

that manganese has a negligible influence on modifying this transformation temperature. The effect of manganese, aluminum and nickel on the transformation temperature is shown in Fig. 10. This suggests that compositional heterogeneity in the weld with rich and lean regions of aluminum and/or nickel could cause a difference in transformation temperatures. The next step is to determine if this compositional heterogeneity exists in the samples before the thermal cycling experiments or if it was introduced during the heating cycles employed for the synchrotron experiment.

Compositional Inhomogeneity in Delta Ferrite Due to Difference in Heating Rates

The instability of the delta ferrite during the faster cooling rate suggests that the substitutional alloy partitioning during the heating cycle which preceded the cooling may have not gone to completion, thus leaving the delta ferrite richer in austenite stabilizers thus pushing the transformation temperatures up during the subsequent cooling cycle.

This hypothesis was tested using Dictra™ by constructing a cell of austenite and heating it to the single phase delta ferrite region and calculating the time taken for homogenization of the composition profile. The prior austenitic grain size in these welds is around 80–100 μm as seen from the optical microstructures. So a 50 μm (half-width of austenite grain size) cell was constructed (Fig. 11a) and austenite was set as the stable phase and heated at a rate of 30°C/s to single phase

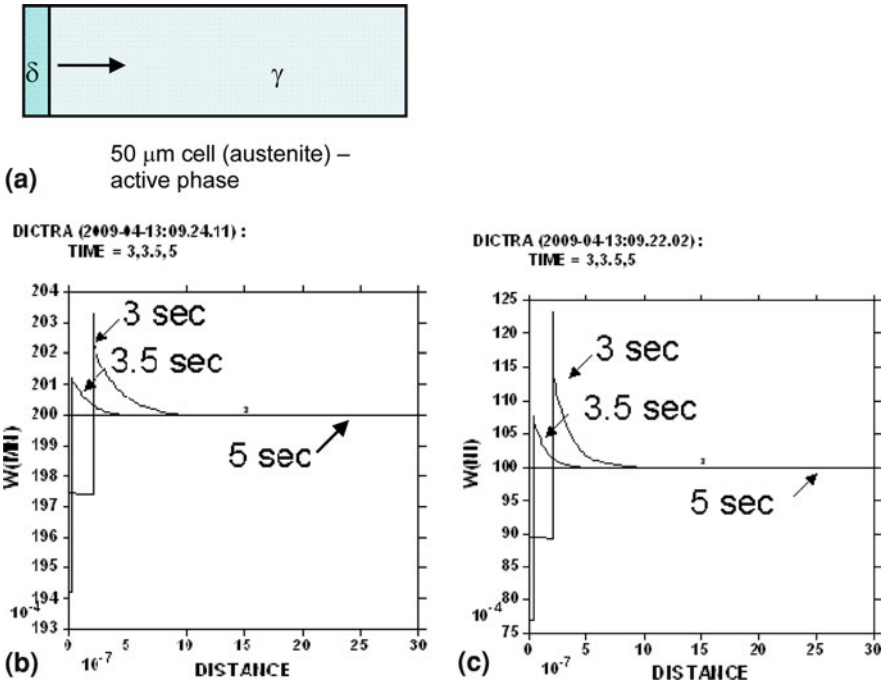

Fig. 11 **a** Schematic of the austenite half cell used for delta to gamma transformation simulation during heating. Simulation results showing the time for homogenization of **b** manganese and **c** nickel in delta ferrite

region of delta ferrite (1450°C). The starting temperature for the simulation was in the single phase austenite region (1300°C). The time taken for the composition profile to homogenize was calculated. Figure 11b and c shows the composition profile of manganese and nickel as a function of distance at three different times (3, 3.5 and 5 s). It is seen that the composition profile homogenizes within 5 s. Even at the faster heating rate (10°C/s) the sample spends, in total, around 24 s in the single phase delta ferrite region. For the slower heating rate (5°C/s) the sample spends around 70 s in the single phase delta ferrite region. This shows that it is unlikely that the heating cycle could cause compositional inhomogeneity leading to a difference in transformation temperatures.

Effect of Cooling Rates on Compositional Heterogeneity

The previous calculation assumes that the parent structure does not possess any compositional inhomogeneity during solidification. This hypothesis was tested by calculating the compositional gradients that could exist due to the fast cooling rates during solidification. Thermocouples were plunged into the weld pool in

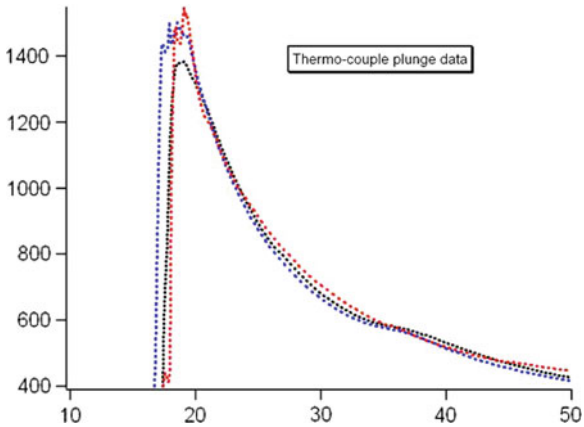

Fig. 12 Cooling rate determination during weld cooling by plunging thermocouples in the weld pool. Plot shows data from three thermocouple plunge traces

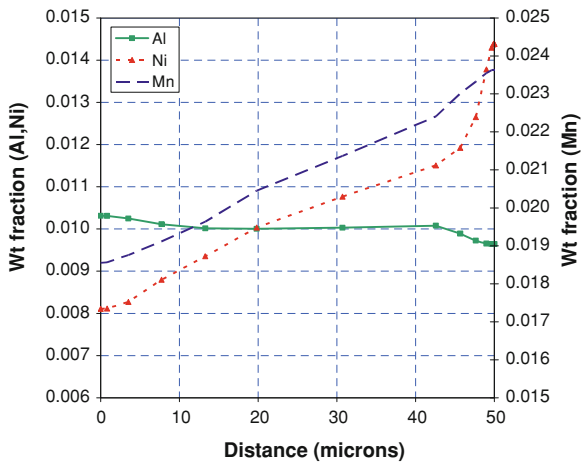

Fig. 13 Effect of fast cooling rates (30°C/s) on composition gradient formation in the weld

order to determine cooling rates for these simulations. The cooling rates were between 100–150°C/s in the delta ferrite stability regions. Figure 12 shows typical cooling curves obtained by thermocouple plunges in the weld pool. Since the delta ferrite phase field is very narrow for the composition of interest, the solidification simulations were carried out using 30 and 100°C/s to check for the effect of cooling rates on the formation of compositional gradients. Both cooling rates showed similar gradients in composition to exist in the delta ferrite. This gradient is shown in Fig. 13. This compositional heterogeneity is tested to understand its effect on transformation temperatures. The effect of this gradient on transformation temperature is shown by introducing an artificial gradient in the delta ferrite and allowing it to transform to austenite. From the earlier simulation experiments shown in Fig. 13, the manganese and nickel gradients were approximated to a linear gradient (1.75% to 2.4% Mn and 0.8% to 1.3% Ni). The aluminum levels were assumed to be constant as it did not show a significant difference across the

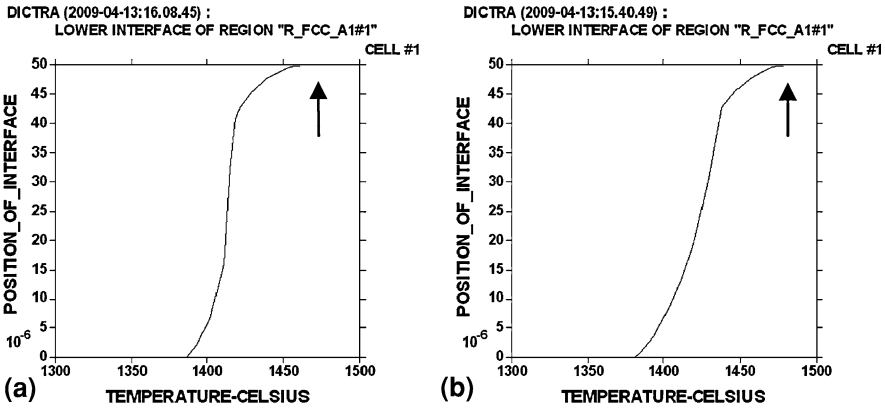

Fig. 14 Simulation of delta to gamma transformation shown in a system **a** without compositional heterogeneity and **b** with compositional heterogeneity shown in Fig. 13. The *arrows* indicate the start of transformation for each case

simulation cell. The effect of this gradient is shown to hasten the transformation by as much as 20°C (Fig. 14).

The composition profile across the simulation cell was tracked as a function of temperature. This compositional heterogeneity survives to a temperature well within the single phase austenite region. It is speculated that at faster heating rate this compositional heterogeneity could survive during the heating experiment introducing instabilities in the delta ferrite thus forcing the transformation to occur at higher temperatures in comparison to the slower heating rate sample which spends a longer cumulative time at a higher temperature and has more opportunity for homogenization.

The as-welded microstructure shows a predominantly bainitic ferrite microstructure with pockets of retained austenite. EDS line profiles across the retained austenitic regions did not show differences in substitutional alloying content to the ferrite. The orientation relationship between the ferritic laths and the prior austenitic grain suggests that the transformation is displacive. These austenitic regions also show evidence of transforming partially to martensite. These suggest that the austenite is unstable and tend to be the nucleation sites for the reverse transformation of the ferrite to austenite during the heating cycle. The microstructures after thermal cycling do not show a statistical difference in the size of the prior austenitic grains. This is consistent with identical austenite to ferrite transformation temperature for the two samples.

EDS scans of the welds after thermal cycling did not show any evidence for segregation of alloying elements to grain boundaries or inter-lath boundaries. The differences in concentrations predicted by Dictra are lower than the resolution limits that can be obtained by EDS in the SEM. Hence it is still conceivable that the chemical inhomogeneities predicted by the simulations still exist and results in a difference in transformation temperatures. The faster cooling rate sample also

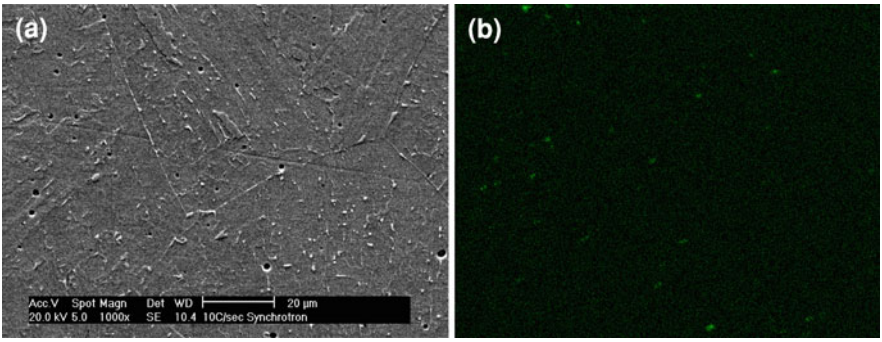

Fig. 15 **a** Secondary electron image of the weld heated and cooled at 10°C/s. **b** Corresponding EDS dot map showing aluminum nitride precipitates

shows aluminum rich clusters correlated to the presence of aluminum nitride inclusions (Fig. 15) indicating that the delta ferrite may have lower aluminum concentrations around these nitride precipitates thus hastening the austenite transformation during cooling.

6 Conclusions

The microstructure of the as-welded region was comprised of prior austenitic grain approximately 80–100 μm in size. The columnar austenitic grains transformed to bainitic ferrite with pockets of retained austenite. All the ferritic grains within a prior austenitic grain conformed to a orientation relationship close to a K–S/N–W O.R. There was no evidence of segregation observed using EDS. However, the weld metal shows small pockets of retained austenite. This suggests that chemical heterogeneity exists in the weld metal leading to stabilization of austenite to room temperature. Two different heating and cooling rates (5 and 10°C/s) were employed and the phase fractions of ferrite and austenite was calculated from the ratio of the peak intensities of the {110} alpha and {111} gamma lattice planes. The different phase transformation temperatures were detected by tracking the phase fraction as a function of temperature during heating and cooling. There was no difference during the heating cycle in the transformation temperatures (alpha to gamma and gamma to delta) and is presumed to be controlled by the pre-existing austenitic pockets acting as nucleation sites for the reverse transformation. However, on cooling the 10°C/s cooling rate sample transformed from delta to gamma at 62°C higher than the 5°C/s cooling rate sample.

Dictra^{TM} was used to simulate the delta to gamma phase transformation assuming diffusion controlled growth of austenite from delta ferrite. The simulation is counter to the measurements from the synchrotron characterization and does not explain the results from the characterization. The most probable reason is

possibly due to compositional inhomogeneity during solidification that was retained to low temperatures. The preferential enrichment of austenite stabilizers in delta ferrite or depletion of ferrite stabilizers could lead to a shift in delta to gamma transformation to higher temperatures. Thermo-calc calculations predict that aluminum and nickel are potent in shifting the transformation temperatures by the amounts seen in the synchrotron measurements.

The possible reasons for locally enriched regions of aluminum/nickel were tested through a series of virtual experiments using Dictra. The results indicated that the chemical inhomogeneity of nickel is possible to be retained to low temperatures due to solidification. It is also possible for nickel enrichment to cause a shift in transformation temperatures of up to 20°C. However, EDS analysis did not show any evidence of nickel inhomogeneity. Locally enriched regions of aluminum were seen in the sample and are attributed to the presence of aluminum nitride inclusions in the weld. It is hypothesized that the regions around the large aluminum nitrides seen in the faster thermal cycle sample may lead to depletion of aluminum around these precipitates that hastens the delta to gamma transformation. Supplemental chemical composition measurements that have better resolution than SEM/EDS is required to corroborate the hypothesis.

References

Andersson JO (2002) Thermo-calc & Dictra, computational tools for materials science. Calphad 26:273

Babu SS (2002) Time-resolved X-ray diffraction investigation of primary weld solidification in Fe-C-Al-Mn steel welds. Acta Mater 50:4763

Babu SS, Elmer JW, David SA, Quintana MA (2002) In situ observations of non-equilibrium austenite formation during weld solidification of an Fe-C-Al-Mn low-alloy steel. Proc R Soc Lond Ser A (Math Phys Sci) (1934–1990) 458:811–821

Babu SS, Elmer JW, David SA, Quintana M (2002b) In situ observations of non-equilibrium austenite formation during weld solidification of an Fe-C-Al-Mn low-alloy steel. Proc R Soc A (Math Phys Sci) 458:811–821

Babu SS, Specht E, David SA, Karapetrova E, Zschack P, Peet M, Bhadeshia H (2005) In situ observations of lattice parameter fluctuations in austenite and transformation to bainite. Metall Mater Trans A 36A:3281–3289

Cullity BD (1978) Elements of X-ray diffraction. Addison Wesley, Reading, MA

Hammersley AP, Svensson SO, Thompson A, Graafsma H, Kvick, Moy JP (1995) Calibration and correction of distortions in two-dimensional detector systems. Rev Sci Instrum 66:2729–2733

Jacot A, Rappaz M (1999) A combined model for the description of austenitization, homogenization and grain growth in hypoeutectoid Fe-C steels during heating. Acta Mater 47:1645–1651

Jimenez-Melero E, van Dijk NH, Zhao L, Sietsma J, Offerman SE, Wright JP, van der Zwaag S (2009) The effect of aluminium and phosphorus on the stability of individual austenite grains in TRIP steels. Acta Mater 57:533–543

Palmer T, Elmer J (2005) Direct observations of the $\alpha \rightarrow \gamma$ transformation at different input powers in the heat-affected zone of 1045 C-Mn steel arc welds observed by spatially resolved X-ray diffraction. Metall Mater Trans A 36:3353–3369

Stone H, Peet M, Bhadeshia HD, Withers P, Babu SS, Specht E (2008) Synchotron X-ray studies of austenite and bainitic ferrite. Proceedings of the Royal Society of London. Series A, Mathematical and Physical Sciences (1934–1990) 464:1009–1027

Thiessen RG, Sietsma J, Palmer TA, Elmer JW, Richardson IM (2007) Phase-field modelling and synchrotron validation of phase transformations in martensitic dual-phase steel. Acta Mater 55:601–614

Wang J, Van Der Zwaag S (2001) Stabilization mechanisms of retained austenite in transformation-induced plasticity steel. Metall Mater Trans A 32:1527–1539